TELKA: Jurnal Telekomunikasi, Elektronika, Komputasi, dan Kontrol
Vol. 12, No. 1, March 2026, pp. 66-78
ISSN (e): 2540-9123 ISSN (p): 2502-1982
DOI: https://doi.org/10.15575/telka.v12n1.66-78

Potential Field Obstacle Avoidance Powered by Grid Certainty Map and Minimum Histogram

Rahmat Zidan[1*], Amalia Prameswari Alvina[2], Putra Wisnu Agung Sucipto[3]
[1,2,3] Department of Electrical Engineering and Informatics, State University of Malang
Building B11, 2nd Floor, State University of Malang, Jl. Semarang 5, Kota Malang
rahmat.zidan.2305366@students.um.ac.id [1*], amalia.prameswari.2305336@students.um.ac.id[2], putrawisnu.ft@um.ac.id[3]

Article Info

Article history:
Received: 07 October 2025
Revised: 03 February 2026
Accepted: 07 February 2026
Published: March 2026

Keywords:
Obstacles;
Tracks;
Histogram;
Maps;
Forces.

ABSTRACT

An omnidirectional robot moving in a crowd of robot soccer players requires autonomous navigation to navigate moving obstacles, generate safe, smooth, and adaptive trajectories when global information is unavailable. Global navigation and local control must be integrated so that spatial memory can balance speed, safety, and smoothness. This study proposes the implementation of Potential Field Obstacle Avoidance (PFOA) with a grid certainty map and a minimum histogram to address these challenges. This idea is based on the repulsive and attractive forces that shape the decision of the direction of motion in PFOA, which need to be accompanied by the confidence of the empty space map in the distribution of obstacle histograms that direct the robot to the right direction. Based on experiments that have been conducted, this approach has proven to perform better than the hybrid A* and bug methods. Our proposed algorithm is able to make the robot's travel time to the target consistently 13-21 seconds, with a smooth motion trajectory due to sharp maneuvers in the most difficult areas that are minimal, and the best safety confidence level value based on the certainty value between the two comparison methods. So it can be concluded that the strengthened PFOA is able to adapt to local dynamics and is superior in planning global robot trajectory maps that contain obstacles.

Corresponding Author:
Rahmat Zidan,
Department of Electrical Engineering and Informatics, Malang State University, Malang, Indonesia
rahmat.zidan.2305366@students.um.ac.id

1. INTRODUCTION

A three wheeled omnidirectional robot operating as a player in robot soccer tournaments functions in environments characterized by complex and dynamic obstacles. Mechanically, this robot offers the advantage of full directional mobility (omnidirectional movement) with highly responsive motion capabilities [1], [2]. However, in practical operation, it requires an intelligent navigation system to regulate efficient movement, particularly in environments where dynamic obstacles dominate over static ones [3], [4]. This system is a critical component, as responsive motion must remain adaptive and robust against potential collision risks.

Designing this robot to perform obstacle avoidance can be approached through various strategies. Based on reactive behavior, Rostami et al. [5] and Antoska-Knights et al. [6] proposed

variations of the Potential Field (PF) method to guide robot motion through the interaction of repulsive forces generated by obstacles and attractive forces directed toward the target. This approach was further adopted by Borenstein and Koren [7] in the introduction of the Vector Field Histogram (VFH) method. On the other hand, Yangqi Ou [8] proposed a global path planner to guide intermediate waypoints of the robot as an alternative navigation strategy. The emphasis lies in the use of heuristic functions and direct cost evaluation to refine grid-based paths, resulting in smoother and more efficient trajectories compared to the standard A* algorithm. These two approaches are important to integrate, considering that VFH and PF are primarily limited to local path regulation and basic attractive-repulsive force interactions. Although they can mitigate sudden obstacle repulsion effects, these methods still rely on instantaneous sensor data and do not account for spatial density distribution or motion history. Without the integration of probabilistic grid mapping or adaptive mechanisms for dense environments, the robot may become trapped in local minima [9], [10]. However, when employing a global planner, the navigation strategy should not rely absolutely on the availability of a complete environmental map or impose excessively high computational demands.

To address these challenges, the Potential Field Obstacle Avoidance (PFOA) algorithm can serve as a viable solution due to its structural simplicity, computational efficiency, and ease of implementation. This approach is still grounded in the fundamental interaction between attractive forces toward the target and repulsive forces generated by obstacles [11], [12]. Illustratively, Figure 1 presents the PFOA field representation.

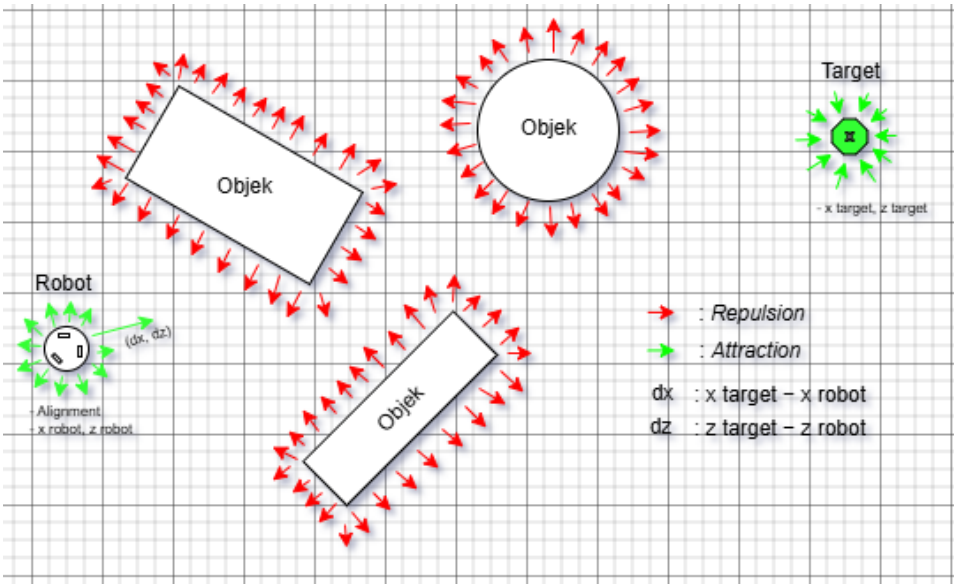

Figure 1. PFOA field.

PFOA offers advantages in terms of a clearer orientation control structure and force parameters that can adapt to environmental changes. However, without the support of grid-based mapping, PFOA still exhibits significant limitations, including inconsistent zigzag trajectories and susceptibility to local minima due to the absence of comprehensive spatial evaluation mechanisms. Therefore, integrating PFOA with a decision-making framework based on grid mapping histogram distribution is considered a promising solution to enhance navigation performance, particularly for three-wheeled omniwheel platforms that require directional flexibility, high maneuverability, and reliable obstacle avoidance in complex environments [13].

This study proposes the integration of the PFOA algorithm with a grid certainty map approach, heading error and heading control mechanisms, as well as a minimum histogram-based decision strategy [14]. The grid certainty map is used to construct a spatial representation of the environment by evaluating the level of certainty of obstacle presence in each grid cell. The

heading error and heading control mechanisms are employed to correct the robot's orientation, while the minimum histogram method determines the safest movement direction based on the historical distribution of the robot's interaction with the mapped environment [15]. The objective is to improve path efficiency and enhance the adaptability of the three-wheeled omniwheel robot in dynamic environments [16]. The main contribution of this study lies in the formulation of a novel certainty value (CV) that integrates heading error and potential forces into the grid representation, along with its incorporation into a minimum histogram-based directional decision mechanism. This approach not only strengthens the reliability of PFOA in addressing local minima and zigzag motion limitations, but also provides a more adaptive framework for navigation evaluation [17].

2. METHOD

The robot navigation system proposed in this study is based on the resultant force field concept of the PFOA algorithm, supported by target-oriented heading control and followed by grid based environmental mapping [18]. This process is accompanied by the computation of the total control signal and the implementation of three-wheel kinematic control. In general, the overall research methodology is illustrated in Figure 2:

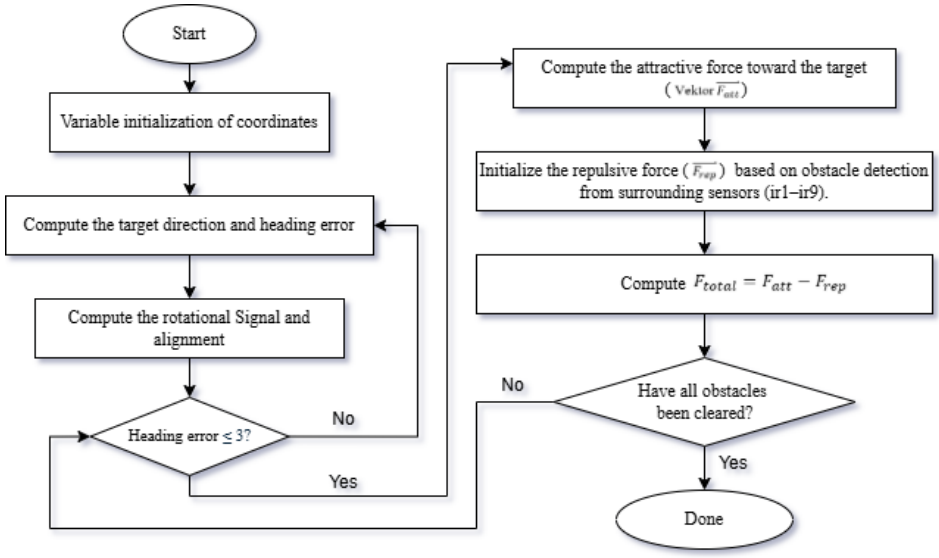

Figure 2. Research methodology.

Figure 2 illustrates the system flow diagram, which can be grouped into four main operational stages: 1) sensor data acquisition; 2) grid based environmental mapping along with clustering and segmentation; 3) construction of the certainty value histogram; and 4) the enhanced PFOA based navigation process.

This navigation process is implemented on a robotic platform equipped with distance sensors distributed circumferentially at 40° angular intervals. Each sensor provides distance measurements to surrounding obstacles [19]. For the purpose of measuring the robot's distance to the target, the robot's global position is monitored in vector form based on the following formulation:

$$dx = x_{target} - x_{robot} \quad (1)$$

$$dz = z_{target} - z_{robot} \quad (2)$$

The values (dx, dz) form a directional vector toward the target and determine the robot's relative position within one of the four Cartesian quadrants.

The robot's heading orientation is calculated based on the geometric direction of the robot's position vector using the following formulation:

$$\theta_{target} = atan2(dz, dx), \quad (3)$$

$$e_\theta = \theta_{target} - \theta_{robot}. \quad (4)$$

Meanwhile, the angular velocity of the robot's heading is calculated using the following formulation:

$$\omega = k_\omega . (-e_\theta), \quad (5)$$

where $k_\omega = 0.8$ represents the rotational gain. The rotational density is calculated based on the alignment between the robot's heading direction and the target direction according to the condition:

$$Alignment = \cos\left(\frac{e_\theta . \pi}{180}\right), \quad (6)$$

The attractive force pulling the robot toward the target is computed using an attractive gain expressed in a two dimensional vector form:

$$F_{att} = k_{att} . \begin{bmatrix} dx \\ dz \end{bmatrix} \quad (7)$$

Meanwhile, the repulsive force generated by obstacles is calculated based on the distance sensor readings using the following formulation:

$$\overrightarrow{F_{rep}} = \sum_{i=1}^{n} k_{rep} . \left(\frac{1}{d_i} - \frac{1}{d_0}\right) . \frac{1}{d_i^2} . \hat{r_i} \quad (8)$$

where $k_{rep} = 0.08$, $d_0 = 1.5$ mdenotes the obstacle influence threshold distance, and $\hat{r}_i$is the unit vector pointing from the obstacle toward the center of the robot.

Equations (9) and (10) represent the robot's position within the motion space, which is categorized into four quadrants. Each quadrant exhibits a dominant directional tendency that supports the navigation strategy. Quadrant I corresponds to forward-right motion, Quadrant II to forward-left motion, Quadrant III to backward left motion, and Quadrant IV to backward-right motion, as illustrated in Figure 3. The geometric orientation vectors of the platform relative to the target are described in Table 1.

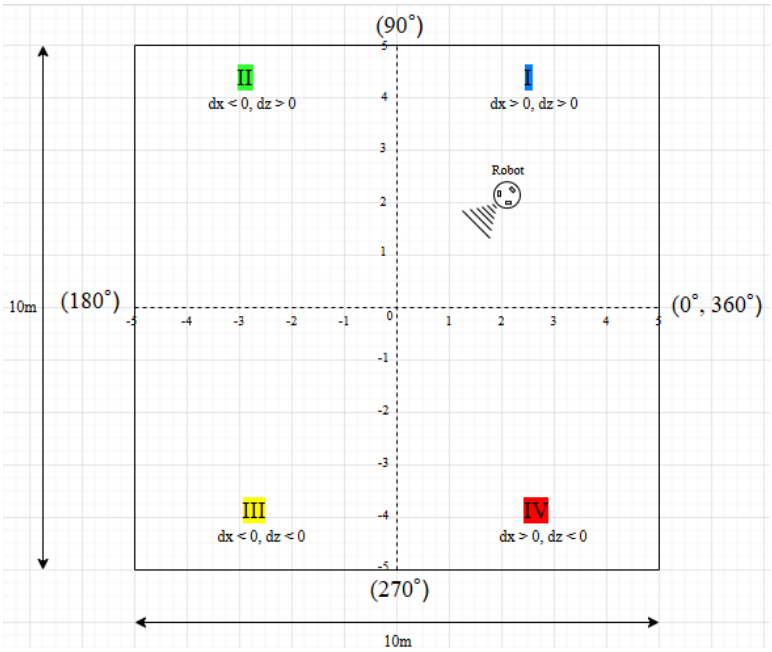

Figure 3. Motion environment quadrants of the robotic platform.

Table 1. Geometric orientation of the robot's heading relative to the target.

Quadran	$\boldsymbol{\theta}$	Robot (x,z)	Vektor ($\vec{\mathbf{v}}$)

I	$0° < \theta \leq 90°$	$dx > \theta, dz > 0$	$(+x, +z)$
II	$90° < \theta \leq 180°$	$dx < \theta, dz > 0$	$(-x, +z)$
III	$180° < \theta \leq 270°$	$dx < \theta, dz < 0$	$(-x, -z)$
IV	$270° < \theta \leq 360°$	$dx > \theta, dz < 0$	$(+x, -z)$

As the platform moves, a certainty map of the motion area is constructed in the form of square grid cells with a constant dimension of $0.1\,m \times 0.1\,m$. Each cell contains a certainty value (CV) indicating the probability of the presence or absence of an obstacle. The CV is formulated based on: (1) heading error; and (2) the intensity of the motion force directed toward the target. The formulation of the CV is given as follows:

$$CV_{Self} = \cos(e_\theta).\frac{\left\|\overrightarrow{F_{att}}\right\|}{\left\|\overrightarrow{F_{att}}\right\| + \left\|\overrightarrow{F_{rep}}\right\| + \epsilon} \tag{9}$$

where e_θ denotes the heading error, $\left\|\overrightarrow{F_{att}}\right\|$ is the magnitude of the attractive force, $\left\|\overrightarrow{F_{rep}}\right\|$ is the magnitude of the repulsive force, and $\epsilon = 0.01$ is a constant introduced to prevent division by zero. Figure 4 illustrates the grid construction and the sensor distribution contributing to the CV value within a grid cell.

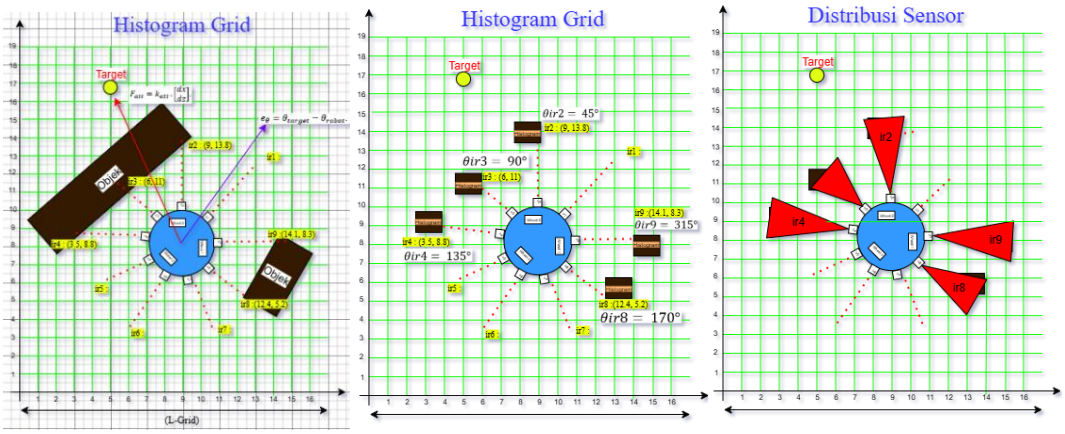

(a) (b) (c)

Figure 4. Grid constructed from CV based (a) object coordinate mapping, (b) classification of sensor scanning angles within the CV grid, (c) and infrared sensor acquisition of objects.

The CV value is directly related to the distribution of distance sensor readings toward obstacle collision points in the Cartesian arena, in order to determine the probability of obstacle presence within a grid cell. The normalization of this probability is defined by the following equation:

$$\Delta CV_i = \frac{d_{max} - d_i}{d_{max} - d_{min}} . CV_{max}, \tag{10}$$

where $d_{max} = 2.0m$, $d_{min} = 0.1m$, and $CV_{max} = 1.0$. Each ΔCV forms an angular histogram sector defined as follows:

$$h_j = \sum_{i \in S_j} \Delta CV, \tag{11}$$

$$h'_k = \sum_{j=-M}^{M} h_{k+j}.\omega_j. \tag{12}$$

Where h denotes the histogram sector, S_j represents the set of cells within sector j, ω_j is the Gaussian weight, and $M = 2$ determines the smoothing widht. Furthermore, based on the condition in (9), the directional risk of the robot's heading can be interpreted by converting CV_{self} into a certainty value risk using the following formula:

$$CV_{risk} = 1 - CV_{Self} \tag{13}$$

If the CV_{self} value is high (corresponding to a histogram peak), it indicates a direction with higher risk. Conversely, a low CV_{Risk} value (corresponding to a histogram valley) reflects a relatively safer environmental condition.

Thus, when the CV is integrated into the repulsive force formulation, it establishes a new condition such that:

$$F'_{rep} = CV \times F_{rep} \tag{14}$$

with the total force vector used to determine the robot's translational direction and velocity expressed as follows:

$$F_{total} = F_{att} - F_{rep} \tag{15}$$

The total force generates valleys with the lowest depth, indicating free space available for robot movement, as well as histogram peaks that represent obstacle density to be avoided. The histogram-based illustration of obstacle peaks and valleys is presented in Figure 5 below:

Figure 5. PFOA field distributions.

3. RESULT AND DISCUSSION

This work has been implemented through simulation using the MATLAB R2022a platform. The robot motion environment was designed as a 10 × 10 meter arena divided into four Cartesian quadrants based on the coordinate axes. Within the arena, a three-wheeled robot equipped with nine infrared sensors for obstacle detection and a GPS module for global position measurement was deployed. The simulation process was conducted over a duration of 30 seconds with a time step of 0.5 seconds. The performance of the proposed method was evaluated using the following metrics: 1) average travel time; 2) number of sharp maneuvers; and 3) average certainty value. The obtained performance metrics were then analyzed comparatively against alternative methods, namely the Bug algorithm [20] and the multistage hybrid A* [21]. Each method is required to navigate the platform from the initial position at (0, 0) toward the target located at (9.5, 9.8) within the arena. During this navigation process, the robot must successfully avoid three different obstacle distribution patterns arranged in the environment. Each obstacle is represented by red lines in the arena.

Based on the experimental results, the proposed method is capable of generating a motion trajectory as illustrated in Figure 6. The resulting path is represented by a blue line, obtained using the parameter settings $k_{att} = 1.0$, $k_{rep} = 0.08$, and an influence radius of $d_\theta = 1.5$. With these parameter configurations, the system produces a translational step size of $h = 0.05$ mand a small damping factor of $damp = 0.03$, while obstacle avoidance is activated through repulsive forces within the influence zone of $d = 1.5$ m. Additionally, the distributions of the repulsive force and heading error throughout the navigation process are presented in Figures 7 and 8, respectively.

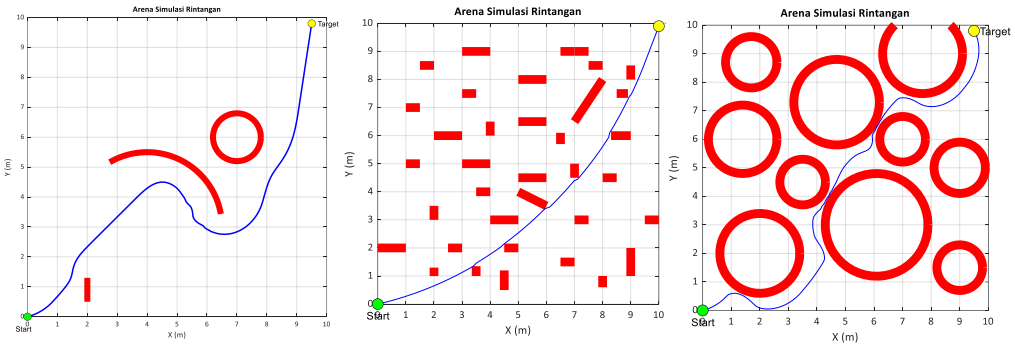

(a) (b) (c)

Figure 6. PFOA robot trajectories in (a) arena 1, (b) PFOA arena 2, and (c) PFOA arena.

In the graph shown in Figure 7, spikes can be observed along the heading error on the y-axis. After passing through a safe valley region where $F_{rep} = 0$, the robot reorients toward the target and the heading error returns to 0°. This heading deviation occurs due to the difference between the robot's actual orientation and the direction of the resultant force F_{total}, which influences how quickly the control system can adjust the heading. The phase characterized by small oscillations at the beginning of the trajectory typically results from angular velocity saturation and the weighting between "maintaining the current heading" and "aligning with the direction of F_{total}." As a result, the curve appears smooth before and after sharp maneuvers around obstacles.

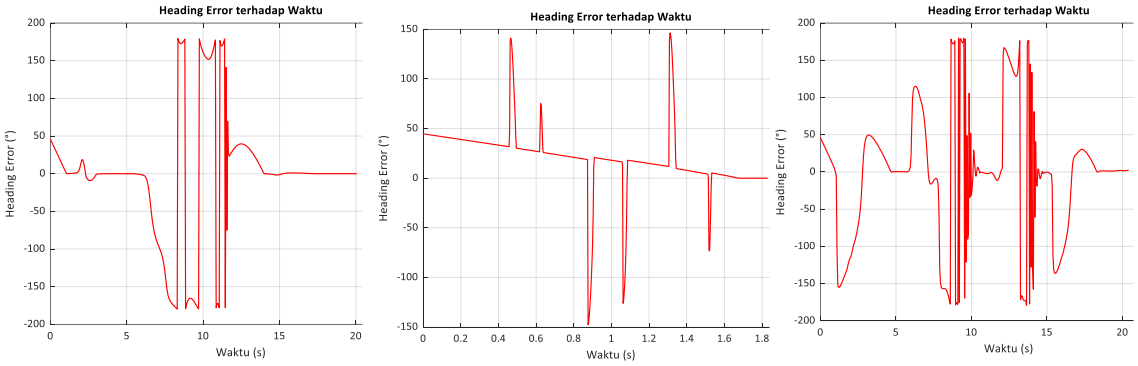

(a) (b) (c)

Figure 7. Heading error distribution of the PFOA method in (a) arena 1, (b) arena 2, and (c) arena 3.

Figure 8 presents three curves distinguished by green, blue, and red colors. The green curve represents F_{att}, which initially has a high value due to the large distance from the target and gradually decreases as the robot approaches the goal. The red curve represents F_{rep}, whose value remains relatively small throughout most of the navigation process but exhibits significant spikes when the robot enters the influence zone of obstacles. The blue curve illustrates F_{total}, showing the combined pattern of $F_{att}$and F_{rep}, which triggers the formation of sectors in the CV histogram during navigation. The F_{total}curve demonstrates that the robot's motion dynamics result from the superposition of attractive and repulsive forces (16), where fluctuations in the blue curve indicate the system's adaptive response to changes in the relative distances among the robot, the target, and the obstacles over time.

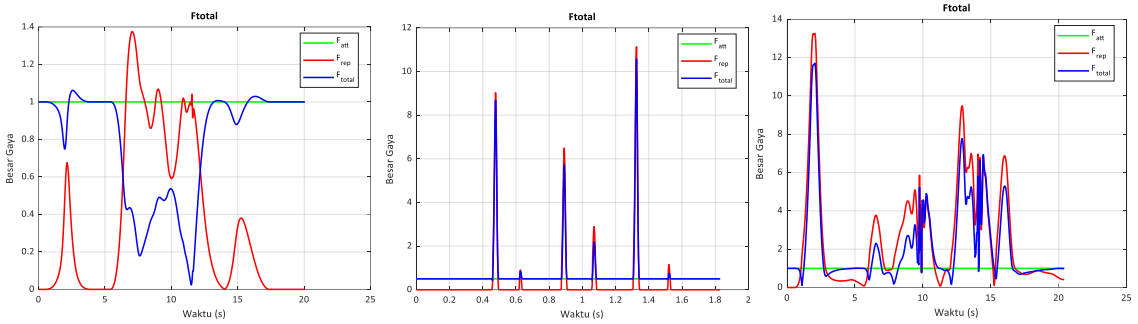

(a) (b) (c)

Figure 8. Force field distribution of the PFOA method in (a) arena 1, (b) arena 2, and (c) arena.

Illustratively, the constructed CV histogram is shown in Figure 9. From the graph, it can be observed that a peak is formed at 230°, with a secondary peak at 155°. The deepest valley appears at 235°, while another low valley is identified at 75°. This peak-valley pattern indicates that the navigation system adaptively selects directions corresponding to the lowest certainty value (CV) regions (valleys) and the most proportionally favorable F_{total} for safe and efficient movement.

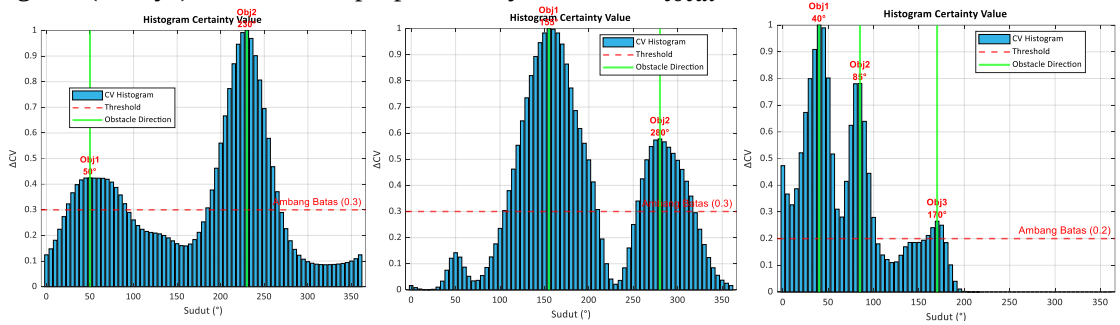

(a) (b) (c)

Figure 9. CV histogram of the PFOA method in (a) arena 1, (b) PFOA arena 2, and (c) arena 3.

When compared with the navigation results generated by the Bug algorithm and Hybrid A* [8], [22], these results show significant differences. The Hybrid A* method employs a total cost function defined as follows:

$$f(n) = g(n) + h(n) \tag{17}$$

where $g(n)$ represents the actual cost from the start node to node n (including travel distance, number of turns, and maneuver penalties), and $h(n)$ denotes the estimated cost from node $n$to the target [23]. The variables $g(t)$, $h(t)$, and $f(t)$ represent deterministic cost functions, where the fundamental conditions are that $g(t)$ must increase monotonically, $h(t)$ decreases as the robot approaches the target, and $f(t)$ changes smoothly in accordance with heuristic consistency. Based on the simulation results, this method is capable of navigating the platform toward the target with an average travel time of 48 seconds over a path length of 14.14 meters, involving an average of eight sharp turns. In Obstacle Scenario 1, the Hybrid A* algorithm produces a fast but rigid trajectory with a travel time of 18 seconds, whereas PFOA follows a smoother and more stable path in 19 seconds. In Obstacle Scenario 2, the performance of Hybrid A* decreases to 26.5 seconds due to the increased number of explored nodes in the narrow arena, while PFOA completes the navigation in 1.82 seconds. In Obstacle Scenario 3, Hybrid A* demonstrates limited adaptability with a travel time of 100 seconds under dense and complex obstacle conditions, whereas PFOA maintains navigation efficiency with a travel time of 21 seconds. Illustratively, the motion trajectories generated by the Hybrid A* method are presented in Figure 10.

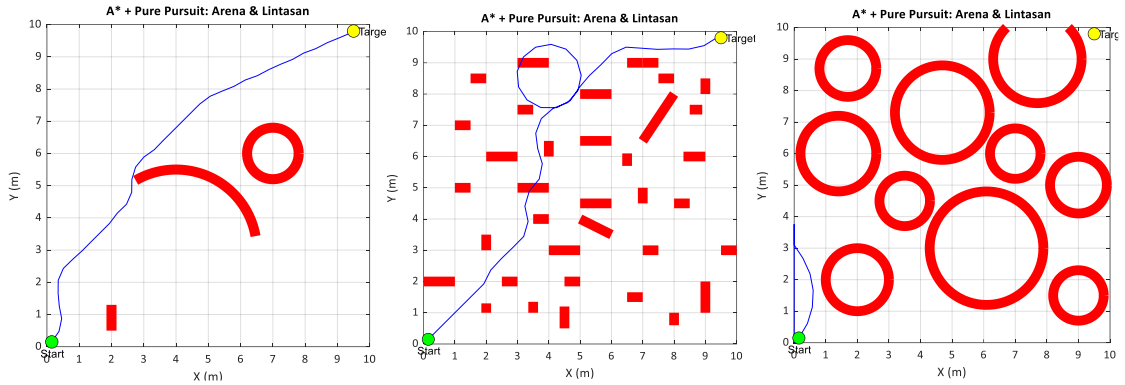

(a) (b) (c)

Figure 10. Robot trajectories based on the hybrid A* method in (a) arena 1, (b) arena 2, and (c) arena 3.

A difference in trajectory patterns can also be observed when compared with the Bug algorithm method [20], [24]. This method operates on the principle of following the outer boundary of obstacles to identify an open path toward the target. Its motion is reactive in nature, combining direct movement toward the goal with obstacle avoidance maneuvers [25]. The direction of motion generated by this method follows the critical point (CP) condition, which is defined by the following equation:

$$v_{CP(t)} = \frac{CP - P(t)}{\|CP - P(t)\|} \tag{18}$$

where $v_{CP(t)}$denotes the directional parameter guiding the robot's motion toward the critical point (CP). The critical point (CP) is defined as the point with the minimum distance to the target, and $P(t)$represents the robot's position at time t. The robot's velocity is maintained at a constant magnitude while its direction continuously adjusts according to the platform's position. This mechanism is employed to maintain motion stability while keeping the robot in close proximity to obstacles. The proposed movement pattern enables the robot to return to a collision-free path without strictly following the obstacle contour, as commonly performed in classical Bug methods [26]. Based on the simulation results, this method is able to navigate the platform toward the target with an average travel time of 19.3 seconds over a 14.14 meter arena, involving an average of seven sharp turns. In Obstacle Scenario 1, the Bug method reaches the target faster, with a travel time of 16 seconds due to the relatively simple obstacle layout, whereas PFOA requires 19 seconds but produces a smoother trajectory. In Arena 2, the Bug method completes navigation in 22 seconds because of repeated maneuvers around barrier walls, while PFOA achieves the task in 1.8 seconds. In Arena 3, the Bug method exhibits numerous sharp turns as a result of its wall-following strategy, whereas PFOA maintains a more consistent movement direction with a travel time of 21 seconds. Illustratively, the motion trajectories generated by the Bug algorithm are presented in Figure 11.

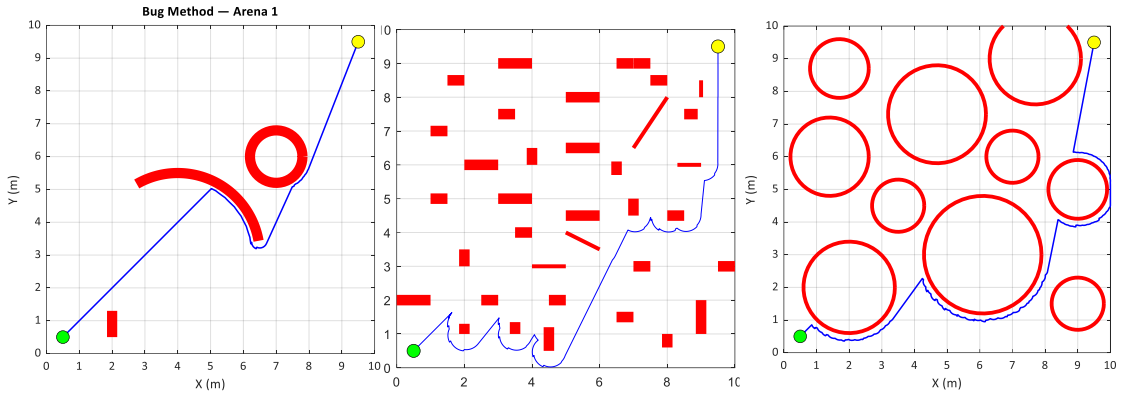

(a) (b) (c)

Figure 11. Robot trajectories based on the bug algorithm in arena 1 (a), bug algorithm arena 2 (b), and bug algorithm arena 3 (c)

Quantitatively, the performance comparison of the three algorithms is summarized in Table 2. The experimental results demonstrate that the proposed PFOA, integrated with a grid based certainty map and a minimum histogram mechanism, effectively mitigates the local minimum problem. Through histogram analysis, alternative navigation directions can be identified when the CV_{risk} exceeds a predefined threshold. Moreover, zigzag patterns during trajectory formation are significantly reduced, as heading control remains relatively stable within $\pm 35°$, which is substantially smaller than the $\pm 60°$ oscillations observed in the Bug algorithm.

Table 2. Simulation data.

Method	Arena	Time (s)	Speed (m/s)	Number of sharp turns	*Clearence Min* (m)
PFOA	1	19.0	0.53	3	0.32
	2	1.8	0.55	2	0.35
	3	21.0	0.52	5	0.31
Bug	1	16.0	0.58	4	0.25
	2	22.0	0.48	7	0.24
	3	20.5	0.50	9	0.23
Hybrid A*	1	18.0	0.56	5	0.30
	2	26.5	0.34	8	0.22
	3	100.0	0.10	12	0.22

The simulation results demonstrate that PFOA maintains stable travel times across all arenas, ranging from 13.9 to 21 seconds, while producing smooth trajectories and consistent orientation. In comparison, the classical local bug method performs faster in simple environments (16 seconds in Arena 1) but generates less optimal paths with up to 9 sharp turns in Arena 3. Meanwhile, the global heuristic hybrid A* approach is efficient in open spaces (18 seconds in Arena 1) but struggles to adapt in dense environments, where travel time increases dramatically to 100 seconds in Arena 3. The certainty value analysis further supports these findings, showing that when $CV_{risk} > 0.8$, the repulsive force component F_{rep} increases by up to 70%, enabling the robot to effectively avoid high risk zones. In terms of safety, the minimum clearance achieved by PFOA is 0.31 meters, exceeding the 0.3 meter safety threshold and outperforming both bug (0.23 meters) and A* (0.22 meters). Nevertheless, this study has several limitations: 1) the simulation scale is restricted to static obstacles; 2) performance is highly dependent on parameter tuning of K_{att}, K_{rep}, and τ_{safe}; and 3) the integration of grid mapping increases computational load by approximately $15-20\%$ compared to the baseline PFOA. Future work will focus on implementation in a physical robot platform with dynamic obstacles, adaptive parameter tuning mechanisms, and computational optimization through selective grid updating. Overall, the

integrated PFOA framework shows strong potential as a navigation strategy for robotic soccer systems requiring a balance between speed, safety, and adaptability.

4. CONCLUSION

The integration of Potential Field Obstacle Avoidance (PFOA) with a grid-based certainty map and a minimum histogram mechanism has been successfully implemented and validated. The proposed system effectively addresses the local minimum trap problem by identifying safe directions through histogram analysis, while trajectory smoothness is enhanced through the integration of a heading control mechanism. Safe navigation is achieved through the certainty value (CV), which combines heading error and the resultant force to detect potentially hazardous directions and appropriately amplify the repulsive force component, ensuring the robot maintains a safe distance from obstacles. In terms of performance, PFOA demonstrates superiority in speed, requiring relatively short travel times to reach the target with only a few sharp maneuvers, while still maintaining adequate clearance from obstacles. Compared to the Bug Method and Hybrid A*, the proposed approach provides a better balance between efficiency, path smoothness, and navigation safety.

ACKNOWLEDGEMENTS

The authors would like to express their sincere gratitude to Universitas Negeri Malang for the financial support through the ”Kompetitif Inovasi Mahasiswa Karya Inovatif” funding scheme, which made it possible for this study to be conducted successfully through to its final stage of publication.

REFERENCES

[1] M. Abreu, L. P. Reis, and N. Lau, *Designing a skilled soccer team for RoboCup: exploring skill-set-primitives through reinforcement learning*, vol. 37, no. 18. 2025. doi: 10.1007/s00521-025-11151-3.

[2] K. Daniilidis and C. Geyer, "Omnidirectional vision: Theory and algorithms," *Proc. - Int. Conf. Pattern Recognit.*, vol. 15, no. 1, pp. 89–96, 2000, doi: 10.1109/icpr.2000.905282.

[3] E. Okta Pratama and Leamongga Chiki, "Sistem Navigasi Pada Robot Sepak Bola Beroda Krsbi Menggunakan Metode Odometry," pp. 1–63, 2019.

[4] P. W. A. Sucipto and A. Firasanti, "Pengendali PID untuk Pengaturan Kecepatan Gerak Robot Omnidireksional Tiga Roda," *TELKA - Telekomun. Elektron. Komputasi dan Kontrol*, vol. 6, no. 1, pp. 66–74, 2020, doi: 10.15575/telka.v6n1.66-74.

[5] S. Mohammad, H. Rostami, A. K. Sangaiah, and J. Wang, "Obstacle avoidance of mobile robots using modified potential field algorithm," *Eurasip J. Wirel. Commun. Netw.*, vol. 2019, no. 1, pp. 1–19, 2019.

[6] V. Antoska-Knights, Z. Gacovski, and S. Deskovski, "Obstacles avoidance algorithm for mobile robots, using the potential fields method," *Univers. J. Electr. Electron. Eng.*, vol. 5, no. 4, pp. 75–84, 2017, doi: 10.13189/ujeee.2017.050402.

[7] L. Schneider, "Real time robot navigation with a smart transducer network," *Master's thesis, Tech. Univ. Wien, Inst. f ur Tech. Inform. Vienna, Austria*, vol. 7, no. 3, pp. 278–288, 2001, [Online]. Available: http://www.vmars.tuwien.ac.at/documents/intern/752/Diplomarbeit_Schneider_Lukas.pdf

[8] Y. Ou, Y. Fan, X. Zhang, Y. Lin, and W. Yang, "Improved A* Path Planning Method Based on the Grid Map," *Sensors*, vol. 22, no. 16, pp. 1–13, 2022, doi: 10.3390/s22166198.

[9] B. Do Kim, C. M. Kang, J. Kim, S. H. Lee, C. C. Chung, and J. W. Choi, "Probabilistic vehicle trajectory prediction over occupancy grid map via recurrent neural network," *IEEE Conf. Intell. Transp. Syst. Proceedings, ITSC*, vol. 2018-March, pp. 399–404, 2017, doi: 10.1109/ITSC.2017.8317943.

[10] T. Kim, J. Kim, and H. T. Choi, "Mobile robot navigation using grid line patterns via probabilistic measurement modeling," *Intell. Serv. Robot.*, vol. 9, no. 2, pp. 141–151, 2016, doi: 10.1007/s11370-015-0191-0.

[11] J. Borenstein and Y. Koren, "Real-time obstacle avoidance for fast mobile robots in cluttered environments," vol. 19, no. 5, pp. 572–577, 1990, doi: 10.1109/robot.1990.126042.

[12] Y. Koren and J. Borenstein, "Potential field methods and their inherent limitations for mobile robot navigation," *Proc. - IEEE Int. Conf. Robot. Autom.*, vol. 2, pp. 1398–1404, 1991, doi: 10.1109/robot.1991.131810.

[13] T. S. Nguyen, H. N. Cao, and M. T. Pham, "Semantic potential field for mobile robot navigation using grid maps," *ETRI J.*, vol. 47, no. September 2024, pp. 422–432, 2025, doi: 10.4218/etrij.2024-0454.

[14] A. N. A. Rafai, N. Adzhar, and N. I. Jaini, "A Review on Path Planning and Obstacle Avoidance Algorithms for Autonomous Mobile Robots," *J. Robot.*, vol. 2022, 2022, doi: 10.1155/2022/2538220.

[15] L. Tang, S. Dian, G. Gu, K. Zhou, S. Wang, and X. Feng, "A novel potential field method for obstacle avoidance and path planning of mobile robot," *Proc. - 2010 3rd IEEE Int. Conf. Comput. Sci. Inf. Technol. ICCSIT 2010*, vol. 9, pp. 633–637, 2010, doi: 10.1109/ICCSIT.2010.5565069.

[16] H. T. and A. Saleem, "Heading Error Shaping Guidance Law for Three Dimensional Impact Time Control," *IEEE Trans. Aerosp. Electron. Syst.*, pp. 1–15, 2025, doi: 10.1109/TAES.2025.3568451.

[17] P. T.-T. Nguyen, D.-D. Nguyen, M.-L. Deng, and C.-H. Kuo, "Improving the Performance

of Visual Odometry for Autonomous Navigation in Environments with Low Illumination and Uneven Terrain," *Int. J. Fuzzy Syst.*, 2025, doi: 10.1007/s40815-024-01930-w.

[18] Y. Kong, W. Yi, and H. Zhang, "Path Planning and Obstacle Avoidance Strategy of Underactuated Dredger Based on Modified Artificial Potential Field," Jun. 01, 2025.

[19] A. Raharjo, E. Kuncoro, I. Azhar, and J. Teknik Telekomunikasi Poltekad Kodiklatad Jl Ksatrian Pusdik Arhanud, "Rancang Bangun Tracking Arah Tembakan Menggunakan Sensor Posisi Berbasis PID Design and Implementation of the Shot Direction Tracking System Using a PID-Based Position Sensor," *Telka*, vol. 7, no. 1, pp. 43–48, 2021.

[20] S. K. Das, K. Roy, T. Pandey, A. Kumar, A. K. Dutta, and S. K. Debnath, "Modified Critical Point - A Bug Algorithm for Path Planning and Obstacle Avoiding of Mobile Robot," *Proc. 2020 IEEE Int. Conf. Commun. Signal Process. ICCSP 2020*, pp. 351–356, 2020, doi: 10.1109/ICCSP48568.2020.9182347.

[21] W. Sheng, B. Li, and X. Zhong, "Autonomous Parking Trajectory Planning with Tiny Passages: A Combination of Multistage Hybrid A-Star Algorithm and Numerical Optimal Control," *IEEE Access*, vol. 9, no. January, pp. 102801–102810, 2021, doi: 10.1109/ACCESS.2021.3098676.

[22] S. Rivat, "On the Heuristics of the Higgs Mechanism," *J. Gen. Philos. Sci.*, vol. 45, no. 2, pp. 351–367, 2014, doi: 10.1007/s10838-014-9258-4.

[23] Y. Xu, G. Guan, Q. Song, C. Jiang, and L. Wang, "Heuristic and random search algorithm in optimization of route planning for Robot's geomagnetic navigation," *Comput. Commun.*, vol. 154, no. February, pp. 12–17, 2020, doi: 10.1016/j.comcom.2020.02.043.

[24] S. S. Divya, A. Nandesh, R. K. Raman, K. Gayathri, and R. Ramanathan, "An Investigation of Bug Algorithms for Mobile Robot Navigation and Obstacle Avoidance in Two-Dimensional Unknown Static Environments," *Proc. - Int. Conf. Commun. Inf. Comput. Technol. ICCICT 2021*, pp. 1–6, 2021, doi: 10.1109/ICCICT50803.2021.9510118.

[25] K. N. McGuire, G. C. H. E. de Croon, and K. Tuyls, "A comparative study of bug algorithms for robot navigation," *Rob. Auton. Syst.*, vol. 121, p. 103261, 2019, doi: 10.1016/j.robot.2019.103261.

[26] N. Sharma, J. Pinto, and P. B. Sujit, "BugFlood: A bug inspired algorithm for efficient path planning in an obstacle rich environment," in *AIAA Infotech @ Aerospace*, in AIAA SciTech Forum. , American Institute of Aeronautics and Astronautics, 2016. doi: doi:10.2514/6.2016-0254.